Available online at www.sciencedirect.com
ScienceDirect
Surface & Coatings Technology 201 (2007) 6977 – 6984
SURFACE & COATINGS TECHNOLOGY
www.elsevier.com/locate/surfcoat

# Modeling of composite coatings in plasma spraying

Qun-bo Fan *, Lu Wang, Fu-chi Wang, Quan-sheng Wang

*School of Materials Science and Engineering, Beijing Institute of Technology, Beijing, 100081, China*

Received 18 October 2006; accepted in revised form 2 January 2007
Available online 13 January 2007

**Abstract**

Based on the mass distribution and dispersion rules for ceramic and metal particles impacting on the substrate, a grid method (GM) has been developed. By combining with the Monte Carlo stochastic model, the GM is successfully employed to simulate the three-dimensional (3D) morphology and the two-dimensional (2D) composition contours of plasma sprayed composite coatings. Instead of considering the complex behavior of the particles impacting on the substrate, the method proposed in this paper directly relates the initial operating parameters to the final morphology of the coatings, including a static gun and a moving gun. This is found to be a very simple but effective way to simulate the composite coatings used in plasma spraying. Through calculating the ceramic mass fraction of each element within the grid, the modeling of the 2D composition contours of the coatings is in good agreement with the SEM experimental results. Up to the present time, similar composition modeling has not been reported elsewhere. Both the methods and the results in this paper may be helpful when analyzing the formation mechanism of the coatings and be of major practical interest in thermal spray operations.


*Keywords:* Numerical simulation; Plasma sprayed composite coatings; 3D morphology; 2D composition contours

## 1. Introduction

Modeling the coating deposition process in plasma spraying, especially that involving different species of powders, is always an interesting but very complex issue. The deposition process is actually an interaction effect between particles of different types, sizes, velocities and molten status on the substrate. High-velocity impaction usually results in splashes of molten particles, while rapid cooling might cause warping of the solidified particles. But not only that, it has been reported that there are two moving interfaces in plasma spraying [1], the moving front of the coating surface, and the subsequently moving liquid–solid two-phase interface, which make such modeling work more difficult.

To simplify the modeling, Chen et al. [2] subdivided the process into two steps: firstly, establishing the related physical models to analyze the behaviors of the single particles on the substrate; and secondly, simulating the coating growth process by integrating all the particles. Zagorski and Stadelmaier [3] employed a simplified thermodynamic droplet model and a statistical model, which successfully simulated the process of the two-dimensional (2D) coating deposition. Such attempts had certain achievements, but they inevitably needed lots of assumptions to describe the various droplet deformations, as well as interactions, and they are not directly related to the initial operating parameters. Thanks to the development of computer science, some comprehensive three-dimensional (3D) computational codes, such as serial products by Simulent Inc. [4] and LAVA3D-P [5], have been developed in recent years to simulate the overall thermal spraying process, as well as the growth of the 3D coatings, in which entrained particles are modeled by stochastic particle models, fully coupled to the plasma flow. Similarly to previous work, there are still a lot of assumptions involved in these codes, dealing with the shape of the droplets, the degree of splattering edge curl up, the porosity of the coating, and so on. In addition, the 2D composition distribution of composite coatings has never been taken into account by these codes.

Based on the modeling results of the plasma jet, jet–particle interaction, and the stochastic particle distributions, with respect to typical experimental conditions, this paper developed a grid

* Corresponding author. Tel.: +86 10 8910 8185.
*E-mail address:* fanqunbo@bit.edu.cn (Q. Fan).

0257-8972/$ - see front matter © 2007 Elsevier B.V. All rights reserved.
doi:10.1016/j.surfcoat.2007.01.011

Table 1
Basic physical properties of powders in plasma spraying

| | Density ($kg/m^3$) | Specific heat (J/kg K) | Thermal conductivity (J/s m K) | Melting point (K) |
|---|---|---|---|---|
| $ZrO_2$ | 5560.0 | 456.1 | 1.85 | 2983 |
| Ni | 8900.0 | 460.6 | 87.86 | 1728 |

method (GM) and combined it with the Monte Carlo stochastic model. In this way, the 3D morphology of coatings and 2D composition distribution of coatings are easily and accurately simulated directly from the initial experimental conditions, instead of being tangled by the details of the spreading droplets.

## 2. Experimental conditions

For comparison with the modeling results, $ZrO_2$ ceramic powders and Ni metal powders were measured and sprayed. The basic physical properties of the two kinds of materials are listed in Table 1. The particle size distribution of the two materials is shown in Fig. 1, and the average size of the $ZrO_2$ powders and Ni powders is 64.5 ìm and 60.5 ìm, respectively. As is well known, in the case of the same sizes and a single injector for both powders, the Ni particles will penetrate more deeply into the plasma jet than the $ZrO_2$ particles due to their relatively higher density, thus causing a poor overlap status for the final ceramic/metal droplets. To ensure a good quality composite coating, the size of the $ZrO_2$ particles is slightly larger than that of the Ni particles.

During the plasma spraying process, a SG100 plasma gun (Praxair-TAFA) and a 1264 powder feeder (Sulzer Metco) were used. Table 2 lists the primary spraying parameters.

## 3. Calculation methods

### *3.1. Modeling procedures of the plasma jet and in-flight particle groups*

For the plasma gun, the input electrical power is equal to the sum of the output powers according to the energy conservation law. The output powers include: the power taken away by the cooling water, the heat power consumed by the plasma gas, as well as the chemical reaction power of the gas [6]. Thus, the temperature at the nozzle exit $T_0$ can be calculated by inputting the initial operating parameters and solving the energy conservation equation, and the velocity at the nozzle exit $V_0$ can also be predicted by calculating the gas state equation [7]. If $T_0$ and $V_0$ are obtained, the temperature and velocity fields of the whole calculation domain can be obtained by solving the equation of mass conservation, the equation of momentum conservation, the equation of energy conservation, as well as the *k*–å turbulence equations [8,9]. Based on such calculations, the relevant particle motion equations and heat transfer models can be added to simulate the heating process and moving behaviors of the particles [10,11]. If the calculation is in a 3D space, the trajectories of the in-flight particle groups and the dispersion status on the substrate can be modeled [12].

Table 2
The primary spraying parameters

| Parameter | Values |
|---|---|
| Primary gas | Ar (70 scf/h) |
| Secondary gas | He (30 scf/h) |
| Arc current | 900 A |
| Spraying distance | 80 mm |
| Powder feed rate | 30 g/min |
| Gun linear velocity | 200 mm/s |

### *3.2. Modeling results of the plasma jet*

Fig. 2 shows the meshed vertical section of the 3D computational domain, with the coordinate origin located at the center of the nozzle exit AB. The nozzle diameter of the plasma gun is 8 mm, and the target stands 80 mm away from the jet in the *Y*–*Z* plane. As illustrated in Fig. 2, the powder port is located axially 8.0 mm downstream from the nozzle exit and vertically 13 mm above the axis of the nozzle. With the initial working conditions listed in Table 2, $T_0$ and $V_0$ at AB will be 13,534 K and 778.2 m/s, respectively.

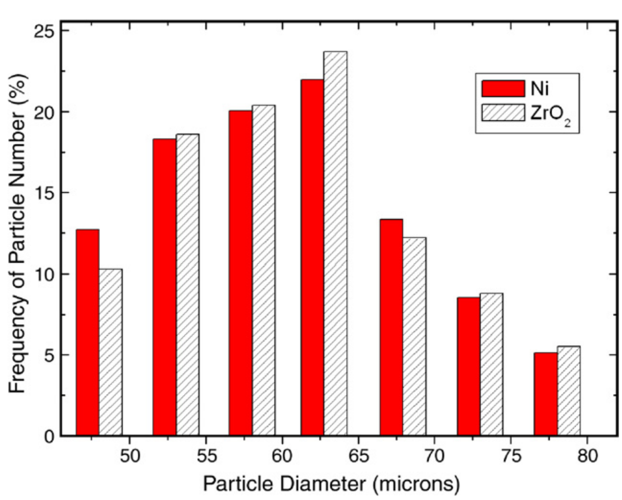


Fig. 1. Size distributions of $ZrO_2$ and Ni particles.

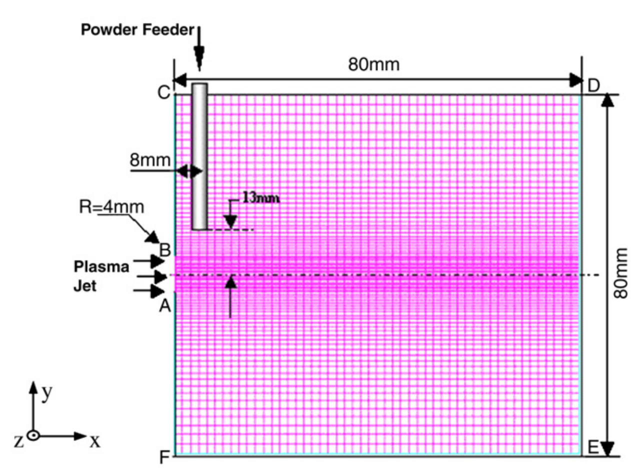


Fig. 2. The calculation domain.

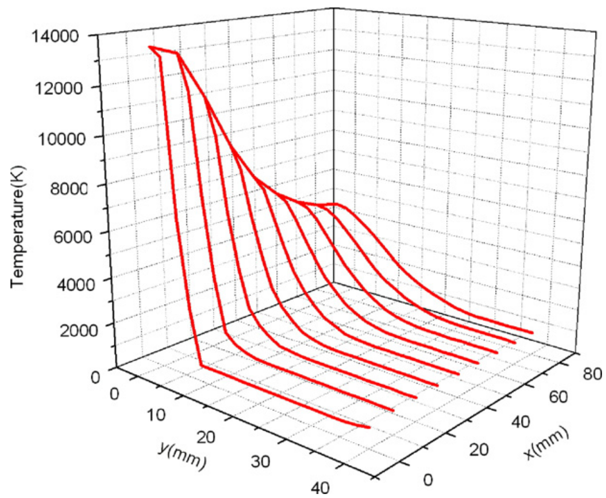


Fig. 3. Temperature field under typical working conditions.

Figs. 3 and 4 show the temperature field and the velocity field under the same initial working conditions, respectively. As can be seen in Figs. 3 and 4, the initial plateau is just the plasma core, indicating that the atmosphere has not penetrated. With an increased axis distance, the temperature and velocity of the plasma jet decrease rapidly due to the entrainment of the atmosphere. But at the outer region far from the plasma core, this effect is considerably weakened.

### 3.3. Modeling results for the particle groups

Fig. 5 shows the space distribution of 50 $ZrO_2$ particles and 50 Ni particles by solving the plasma jet–particle interaction equations. Fig. 5(a) presents the particle trajectories and Fig. 5(b) shows the corresponding particle disperse distribution on the substrate. It can be seen that the turbulent fluctuation of the plasma jet has such a significant effect on the particle trajectories that the particles distribute randomly and stochastically in the 3D space. It might be noted, however, that we can still see that the Ni particle group penetrates more deeply into the plasma jet due to the relatively larger density as mentioned in Section 2, though they can partially overlap with each other.

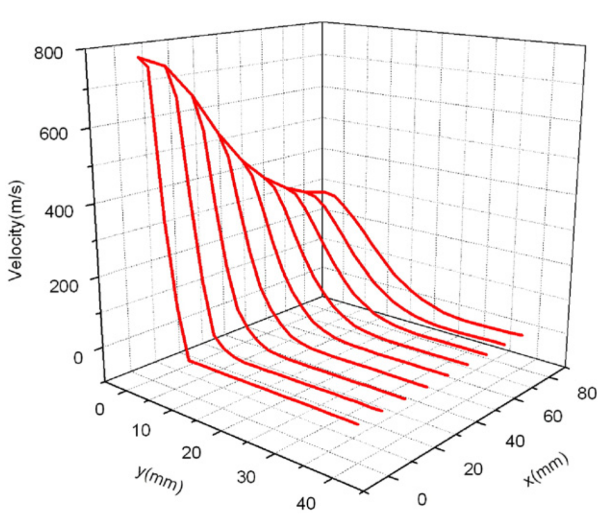


Fig. 4. Velocity field under typical working conditions.

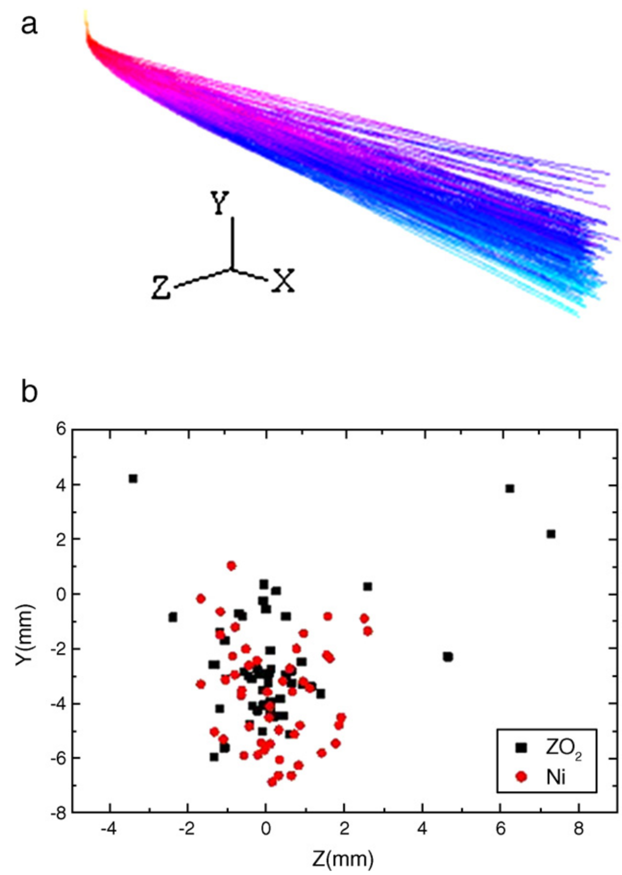


Fig. 5. Space distribution of 50 $ZrO_2$ particles and 50 Ni particles. (a) Particle trajectories in 3D space. (b) Particle distribution on the substrate surface.

### 3.4. GM and stochastic model

When calculating the dispersion status of the particles, given that there are millions of particles on the substrate, it would be rather expensive and complex to compute it. Therefore, we developed a method called the GM to generate new particles. In this way, an $N \times N$ grid is divided on the selected micro-zone of the substrate, and then new particles are generated by using a stochastic model. Each element of the grid is initially assigned an element number $[i][j]$, where $i$ represents the row number of the grid, and $j$ represents the column number of the grid. In the

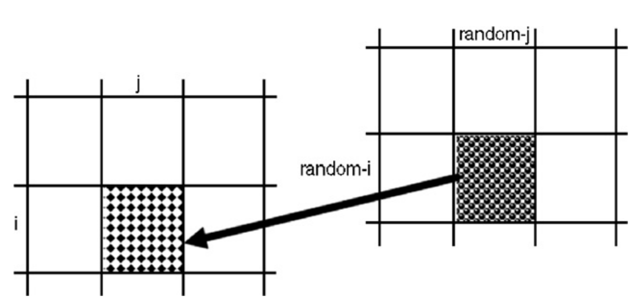


Fig. 6. Schematic diagram of one stochastic operating process.

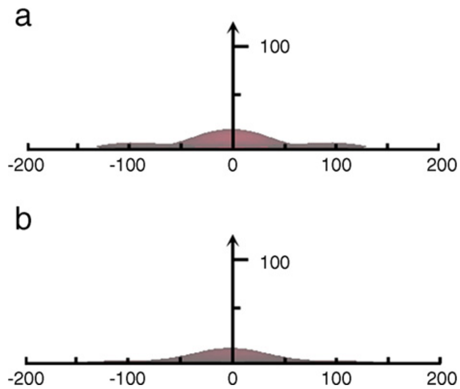


Fig. 7. The spreading shape of a single droplet impacting onto the substrate. (a) A solidified $ZrO_2$ droplet with an initial diameter of 64.5 μm; (b) a solidified Ni droplet with an initial diameter of 60.5 μm.

subsequent stochastic operating process, there is a total of $N \times N$ random numbers with the element number [random-*i*][random-*j*] generated, and each random number is superimposed onto the original element order, as illustrated in Fig. 6. Such a process is called a stochastic operating process, which means that the particle numbers in the element [random-*i*][random-*j*] generated in each stochastic operating process are added to the element [*i*][*j*], thus enriching the total number of particles. Since the dispersion status of the initial particles in each element is calculated strictly by solving the relevant governing equations mentioned in Section 3.1, the dispersion status of the newly generated particles will remain constant, with almost the same mass distribution, diameters, and species distribution status. In this paper, the Monte Carlo model [13] is used as the stochastic model.

For the simulation of discrete random variables, the nature of the Monte Carlo model is: to simulate a random number $X$, its distribution law needs to be known, so as to generate a series of probable value $x_i$ ($i=1, 2, \ldots$). Meanwhile, the random variable $R$ is introduced, satisfying a continuous distribution between 0 and 1; and $r_j$ ($j=1, 2, \ldots$) is the probable value of $r$.

Therefore, to simulate the following discrete distribution

$$\begin{array}{lll} X & x_1 & x_2 \ldots x_n \\ R & p_1 & p_2 \ldots p_n \end{array}$$

where $p$ is the corresponding probability of the variable $x$, then

1) The interval (0, 1) on the $\vec{\ }or$ axis is divided into $n$ sections: $\Delta_1-(0,\ p_1)$, $\text{Ä}_2-(p_1,\ p_1+p_2)$,..., $\text{Ä}_n-(p_1+p_2+\ldots p_{n-1},\ 1)$
2) Select the random number $r_j$.

If $r_j$ is located in the interval section $\Delta_i$, then $x_i$ will be the stochastically generated value.

### 3.5. Determination of 3D coating morphology and 2D composition distribution

The size of each element in the gird will directly affect the calculation of the final results. If the element size is overlarge, it would be difficult to evaluate the height of the coating by simply taking into account the particle stacking effect. If the element size is oversmall, the spreading effect of the molten droplets will inevitably be ignored. Therefore, the determination of the element size should be based on the actual spreading morphology of each droplet.

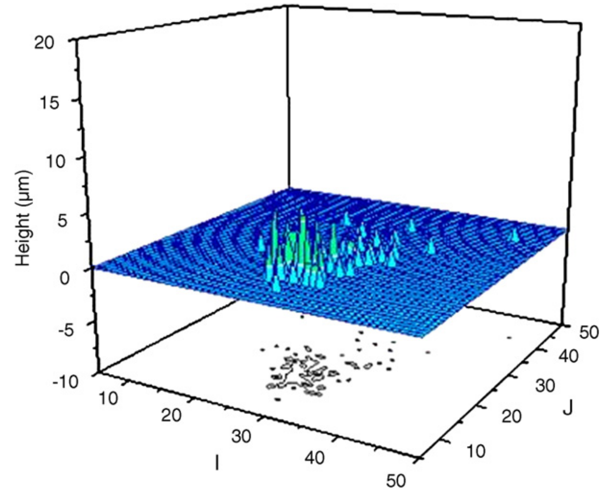


Fig. 8. 3D morphology of 100 ceramic particles when the plasma gun is held static relative to the substrate.

Fig. 7(a) shows a typical final spreading shape of a solidified $ZrO_2$ droplet with an initial diameter of 64.5 μm; Fig. 7(b) shows the typical final spreading shape of a solidified Ni droplet with an initial diameter of 60.5 μm. The final diameter of a solidified splat is about four times as large as the original diameter of a particle, which is in good agreement with the experimental observations. The related mathematical models and calculation details have been reported elsewhere [14].

Based on the spreading shape of the droplets, it is proposed that the element size accords with the following rules: the area of each element should be slightly larger than the full spreading area of a single droplet so as to contain a single solidified

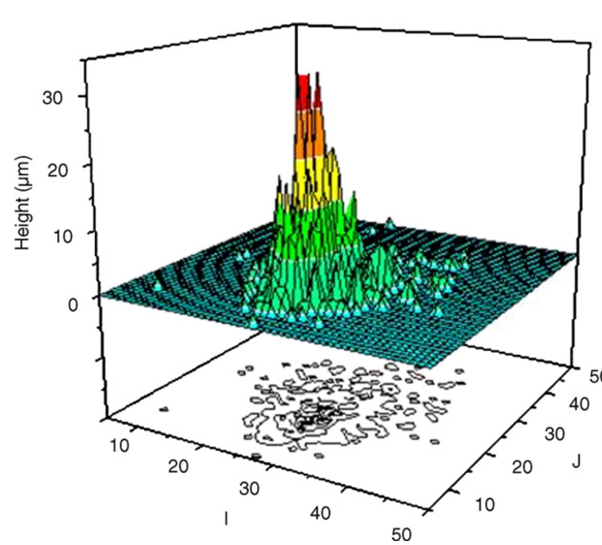


Fig. 9. 3D morphology of 1000 ceramic particles when the plasma gun is held static relative to the substrate.

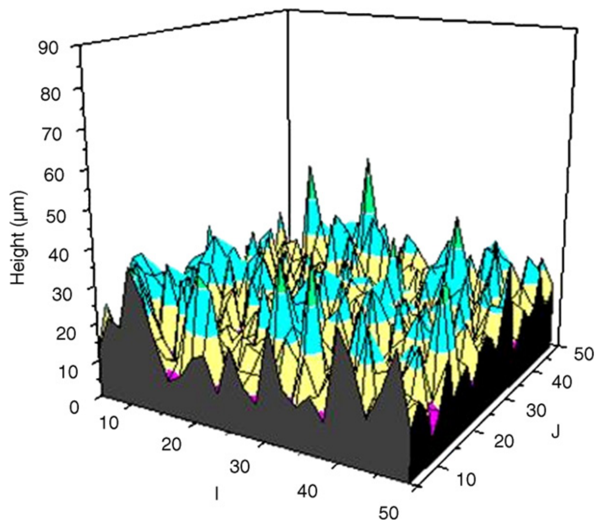


Fig. 10. 3D morphology of 100% $ZrO_2$ ceramic coating.

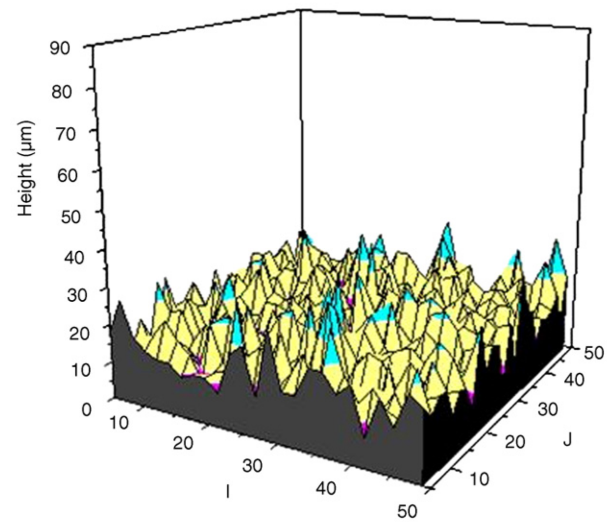


Fig. 12. 3D morphology of 100% Ni ceramic coating.

particle, and ensure that the subsequent droplets deposit on its top. Thus, particle $n$ should be located on the $n$th layer within the same element. On the basis of the above rules and the particle dispersion status illustrated in Fig. 5(b), this paper simulated the coating morphology on a 8 mm × 8 mm substrate surface, and meshed it into 50 × 50 elements.

Using the GM and the stochastic model, the randomly generated $ZrO_2$ ceramic particle numbers and the Ni metal particle numbers are stored in the matrixes $C_0[i][j]$ and $M_0[i][j]$, respectively. Thus, the coating thickness $H[i][j]$ in the grid element $[j][j]$ can be expressed in the following form:

$$H[i][j] = C[i][j] \times \overline{h}_2 M[i][j] \times \overline{h}_M$$

where, $\overline{h}_c$ and $\overline{h}_M$ are the average heights of the spreading droplets shown in Fig. 7. In this way, the thickness of the local coating is characterized by the sum of the heights of all the solidified particles within the corresponding elements.

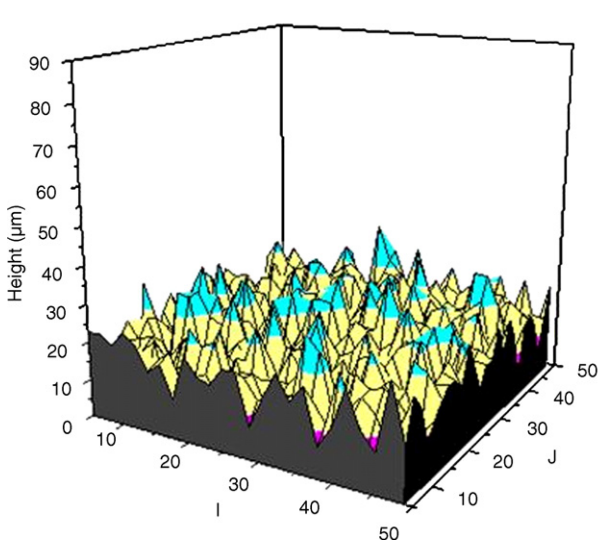


Fig. 11. 3D morphology of 53.9% $ZrO_2$ ceramic coating.

The element mass fraction $M_f[i][j]$ of $ZrO_2$ ceramic particles is determined by:

$$M_f[i][j] = M_c[i][j]/(M_c[i][j] + M_M[i][j])$$

where, $M_c$ and $M_M$ are the total mass of the $ZrO_2$ particles and the total mass of the Ni particles inside the grid element $[i][j]$, respectively. Based on the value of $M_f[i][j]$, the 2D mass fraction contours can be plotted.

It might be noted that the porosity formation and the heat of propagation are not taken into account in this paper, so as to simplify the calculations. The relevant work will be conducted in further studies. In addition, since the input power is relatively higher, it is assumed that most of the particles are completely molten.

## 4. Results and discussion

### 4.1. 3D morphology of the coating

Based on the models presented in this paper, when modeling the 3D morphology of the coating, the stochastic operating number should be defined before the calculation is done. Setting the stochastic operating number has two effects: one is to enrich the data information within each element; the other is to simulate the spraying gun moving homogeneously above the substrate since the composition of the coating is kept the same as the initial dispersion status if employing the stochastic model. If the stochastic operating number is set as 0, then the locations of the particles can be directly calculated by solving the governing equations as mentioned in Section 3.1, which just reflect a spraying process with the plasma gun held static relative to the substrate.

#### 4.1.1. Coating morphology when the plasma gun is held static relative to the substrate

Figs. 8 and 9 show the coating 3D morphology and corresponding height contours when the plasma gun is static

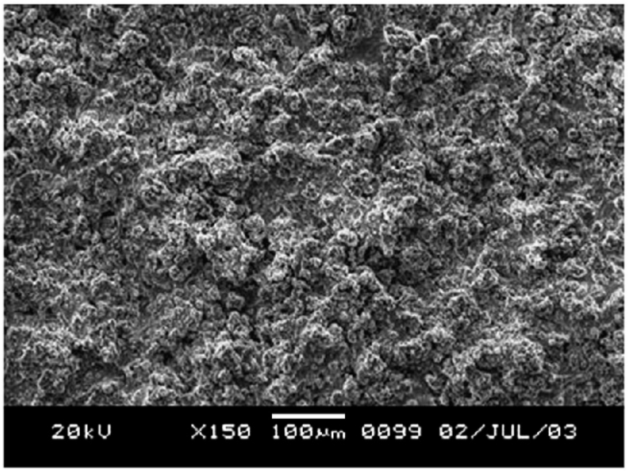


Fig. 13. SEM photograph of 50% $ZrO_2$ coating.

relative to the substrate, with the same initial parameters as mentioned in Section 2. Fig. 8 shows a total of 100 $ZrO_2$ ceramic particles, and the maximum height is 7.37 μm; in Fig. 9, there are 1000 $ZrO_2$ ceramic particles in total, and the maximum height is 33.2 μm. As can be seen in Figs. 8 and 9,

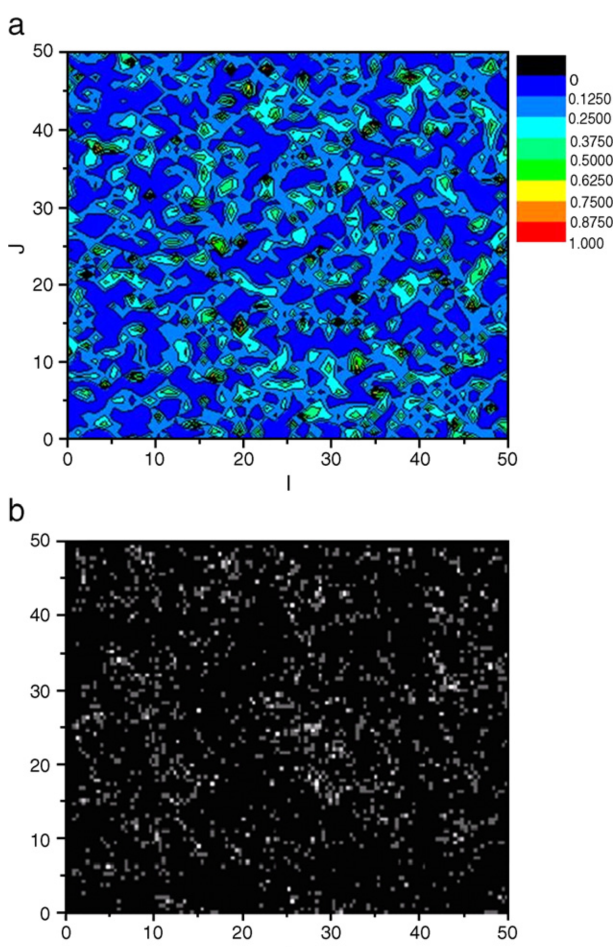


Fig. 14. 2D composition contours of $ZrO_2$–Ni coating with 16.4% $ZrO_2$. (a) Simulated results; (b) SEM experimental result of Zr component contribution. (For interpretation of the references to color in this figure legend, the reader is referred to the web version of this article.)

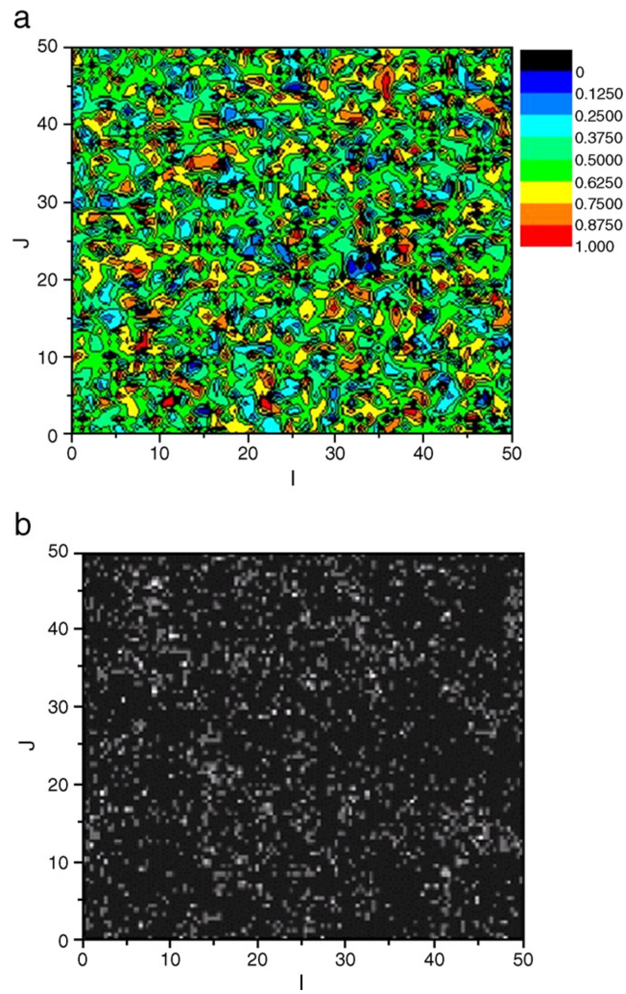


Fig. 15. 2D composition contours of $ZrO_2$–Ni coating with 53.9% $ZrO_2$. (a) Simulated results; (b) SEM experimental result of Zr component contribution. (For interpretation of the references to color in this figure legend, the reader is referred to the web version of this article.)

when the plasma gun is static, the particle group always deposits around a certain location, although the covered area on the substrate increases with the addition of the newly generated particles. As more and more particles are deposited, the coating will become thicker and thicker, which is in good agreement with practical spraying operations.

*4.1.2. 3D morphology of coatings with different compositions*

In practical plasma spraying, the plasma gun is usually moving homogeneously in each direction so as to obtain an equi-thickness coating. To obtain sufficient data within each element, the number of initial particles is 100, and the stochastic operating number is 250, with the same operating parameters as mentioned in Section 2.

Figs. 10–12 show the 3D morphology of 100% $ZrO_2$, 53.9% $ZrO_2$, and 100% Ni coatings, respectively. After 250 stochastic operations, the initial 100 particles will become 25,000 particles. In Fig. 11, the original number of particles for both $ZrO_2$ and Ni is 50, but the mass fraction of $ZrO_2$ is 53.9% because its density is different from that of Ni. In addition, Figs. 10–12 show that the composition of each coating is

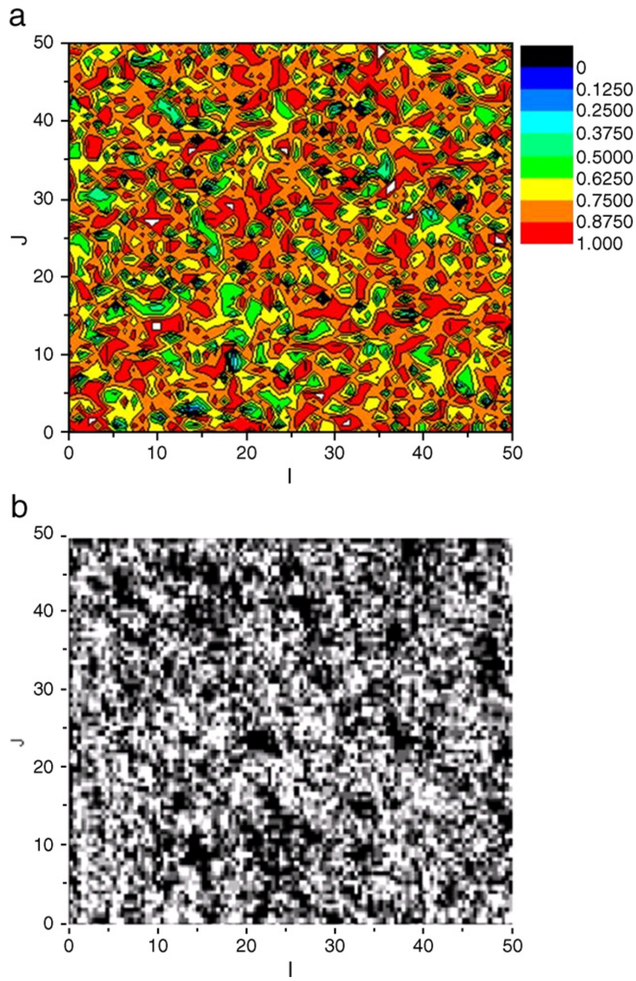


Fig. 16. 2D composition contours of $ZrO_2$–Ni coating with 75.7% $ZrO_2$. (a) Simulated results; (b) SEM experimental result of Zr component contribution. (For interpretation of the references to color in this figure legend, the reader is referred to the web version of this article.)

different, and the thickness of the 100% $ZrO_2$ coating (18.6 μm) is relatively higher than that of the 100% Ni coating (15.1 μm), since the initial average diameter of the $ZrO_2$ droplet is slightly larger than that of the Ni droplet (see Section 2). Therefore, with increasing the $ZrO_2$ composition for a $ZrO_2$–Ni coating, the thickness of the coating will increase. In addition, Figs. 10–12 show that the surface of the coating is rough, which is consistent with the experimental results. Fig. 13 shows the SEM photograph of a 50% $ZrO_2$ coating in mass fraction. From the viewpoint of calculation, the roughness results from the different particle types, numbers, and sizes within each element.

### 4.2. 2D composition contours of the coating

Figs. 14–16 show the composition contours of 16.4% $ZrO_2$, 53.9% $ZrO_2$, and 75.7% $ZrO_2$ coatings in the *Y–Z* plane, respectively. Figs. 14(a), 15(a) and 16(a) present the simulated results, in which the different colors represent the different mass fractions of $ZrO_2$. Figs. 14(b), 15(b) and 16(b) present the SEM experimental results of the Zr component contribution on the surface of the coatings, in which the white and light areas represent the Zr element, indirectly reflecting the distribution status of $ZrO_2$. All the initial operating parameters are the same as those mentioned in Section 2.

As presented in Figs. 14–16, the numerical simulation results are in good agreement with the experimental results. The composition contours of each coating are different for different $ZrO_2$ mass fractions. The results show that even if in the same coating, the compositions in different local areas are also different, but the composition of the same coating fluctuates near the predefined value. Using the numerical analysis of the simulated results, it can be found that the average ceramic composition at the centerline of the coating is 16.3%, 59.5% and 76.2%, respectively, approaching the original mass fractions of $ZrO_2$. Such results confirm that the methods proposed in this paper correctly describe the formation process of the composite coatings.

## 5. Conclusion

By establishing a grid method and employing the Monte Carlo stochastic model, the 3D morphology and 2D composition contours of the composite coating have been successfully modeled. The main results are summarized as follows: (1) through inputting the initial operation parameters and solving the governing equations of the turbulent plasma jet and in-flight particles, the dispersion status of the $ZrO_2$ and Ni particles on the substrate is obtained. (2) Based on the dispersion of the droplets, more ceramic and metal particles are generated by employing the Monte Carlo stochastic model. The 3D morphology and 2D composition contours of the coatings are simulated by counting the thickness and mass fraction of each grid element. (3) Compared with traditional coating growth models, this paper avoids the traditional redundant presumptions, such as the complex and spreading rules about the spreading droplets, making the calculated results simpler and more reliable. Moreover, the models in this paper are directly related to the initial working conditions. (4) Although the porosity and the heat of propagation of the coating are not taken into account, the method proposed in this paper is still theoretically helpful to further investigate the formation process of composite coatings and to optimize the quality of the coatings in the future.

## Acknowledgement

This work was supported by the Excellent Young Teacher Foundation of Beijing Institute of Technology under Contract 1040012040101.

## References

[1] J.W. McKelliget, G. Trapaga, E. Gutierrez-Miravete, M. Cybulsky, in: C. Coddet (Ed.), Thermal Spray: Meeting the Challenges of the 21st Century, vol. 1, ASM International, Materials Park, OH, USA, 1998, p. 335.
[2] Y. Chen, G. Wang, H. Zhang, Thin Solid Films 390 (2001) 13.
[3] A.V. Zagorski, F. Stadelmaier, Surf. Coat. Technol. 146–147 (2001) 162.
[4] www.simulent.com [Online].

[5] G. Wei, H. Xiong, L. Zheng, H. Zhang, An advanced ceramic coating buildup model for thermal spray processes. Thermal Spray: Advances in Technology and Application, Published by ASM International, Materials Park, OH, USA, May 10–12, 2004, p. 707.
[6] Q. Fan, L. Wang, F. Wangm, J. Beijing Inst. Technol. 13 (1) (2004) 80.
[7] Y.Y. Zhao, P.S. Grant, B. Cantor, Modell. Simul. Mater. Sci. Eng. 8 (4) (2000) 497.
[8] R. Bolot, M. Imbert, C. Coddet, in: C.C. Berndt (Ed.), Thermal Spray: A United Forum for Scientific and Technological Advances, ASM International, Materials Park, OH, USA, 1997, p. 549.
[9] P. Eichert, C. Coddet, M. Imbert, in: C.C. Berndt (Ed.), Thermal Spray: Practical Solutions for Engineering Problems, ASM International, Materials Park, OH, USA, 1996, p. 563.
[10] Y.M. Yang, C. Coddet, M. Imbert, in: C. Coddet (Ed.), Thermal Spray: Meeting the Challenges of the 21st Century, Vol. 1, ASM International, Materials Park, OH, USA, 1998, p. 431.
[11] P.C. Huang, J. Heberlein, E. Pfender, Surf. Coat. Technol. 73 (3) (1995) 142.
[12] I. Ahmed, T.L. Bergman, J. Therm. Spray Technol. 9 (2) (2000) 215.
[13] J.E. Gentile, Random Number Generation and Monte Carlo Methods, Springer Verlag, New York, 1998.
[14] Qunbo Fan, Lu Wang, Fuchi Wang, Mater. Mech. Eng. 26 (7) (2002) 19.